CFD Assessment of Directional Wind Loads and Pedestrian-Level Wind Microclimate for a High-Rise Office Complex on Reclaimed Coastal Terrain in Lagos, Nigeria

Desmond Iorhemen Abi[1], Aleksandra Kupreeva[1], Abdulakeem O. Ayuba[1], Oranderen. M. Mzough[1]

Department of Applied Mathematics and Computational Modelling in Construction, Moscow State University of Civil Engineering (MGSU), Yaroslavskoye Shosse 26, Moscow 129337, Russia
Corresponding Author E-mail: abidesmondfalex@gmail.com

Abstract

High-rise structures located on open, low-roughness coastal land are subjected to unobstructed wind flows that generate strong aerodynamic loads and potentially hazardous pedestrian-level wind environments. This study presents a direction-resolved Computational Fluid Dynamics (CFD) investigation of wind loading and pedestrian-level wind comfort for a 104 m tall office tower forming part of a stepped administrative complex on Victoria Island, Lagos, Nigeria. Simulations were executed using steady Reynolds-Averaged Navier-Stokes (RANS) equations with the Generalized k-ω (GEKO) turbulence closure in Ansys Fluent. A dual-domain computational framework (an inner cylindrical domain and an outer rectangular domain) enabled 360° directional evaluation across sixteen 22.5° wind sectors by rotating the outer domain interface. Aerodynamic force coefficients (CFx, CFy, CFR) and moment coefficients (CMx, CMy, CMR) were derived across all directions. The critical loading sectors were identified at 315° and 337.5° for maximum resultant shear force coefficients (CFR = 0.88), and at 180° for maximum overturning moment coefficient (CMR = 0.61), aligning closely with dominant regional onshore wind vectors. Quantitative pedestrian-level flow evaluations based on Lawson (LDDC) comfort criteria reveal high-velocity corner streams and downwash acceleration corridors around the tower base (M = U/Uref > 1.3), indicating potential localized discomfort during peak operational conditions. Recommendations are outlined for facade structural design, mitigation through local canopy interventions, and grid-sensitivity protocols.

Keywords: *Computational Fluid Dynamics (CFD); Atmospheric Boundary Layer; Tall Building Aerodynamics; Aerodynamic Force Coefficients; Pedestrian Wind Comfort; Coastal Exposure; GEKO Turbulence Model.*

Highlights

- Direction-resolved steady-RANS CFD of a 104 m coastal tower over 16 wind sectors.
- Peak resultant force coefficient CFR = 0.88 at 315°; moment CMR = 0.61 at 180°.
- No-slip walls with a power-law ABL inlet and matched k–ω turbulence profiles.
- Pedestrian corner streams reach M = U/Uref up to 1.52 (Lawson Category D).
- Load coefficients rise with height; corner canopy mitigation is recommended.

1. Introduction

Wind excitation is a primary governing environmental action in the structural design and microclimatic assessment of tall buildings, and wind-induced damage to the built environment continues to cause substantial economic and safety losses worldwide [1, 2, 47]. As atmospheric boundary-layer (ABL) flow impinges on a bluff high-rise structure, flow separation, vortex shedding and downward flow deflection develop along the windward facade, producing non-uniform surface pressures, dynamic base shear and overturning moments, and high-velocity jets at ground level that can impair pedestrian safety and comfort [3, 4, 49]. Because these effects intensify with building height and with the openness of the upstream terrain, both the envelope loading and the pedestrian-level wind field must be resolved direction-by-direction for slender towers in exposed settings [5, 6].

Computational fluid dynamics (CFD) with Reynolds-Averaged Navier-Stokes (RANS) closures is now an established complement to boundary-layer wind-tunnel (BLWT) testing for wind-load estimation and pedestrian-level wind assessment, providing whole-field pressure and velocity data at comparatively low cost [7, 8, 9, 25, 51]. Its credibility, however, hinges on adherence to community best practice: adequate domain size, demonstrated grid independence, higher-order discretization, an appropriate turbulence closure, and a horizontally homogeneous ABL inflow [10, 11, 12]. Benchmark reviews for pedestrian wind and for high-rise wind loads consistently report that steady RANS predicts mean loads and high-amplification pedestrian velocities well, whereas large-eddy simulation is more accurate in separated and low-speed regions [5, 13, 14, 15].

The aerodynamics of high-rise buildings in dense urban and interfering-building configurations are extensively documented, including the influence of surrounding structures, plan shape and corner geometry on the pressures, forces and pedestrian-level wind field [16, 17, 18, 19, 20, 21, 43, 44, 45, 46, 50].

By contrast, comparatively little CFD work addresses high-rise development on open, low-roughness coastal terrain typical of West African cities, where a tall building can stand in near-isolation and the reclaimed, low-lying ground offers little shelter. Existing coastal and tropical studies have examined pedestrian ventilation in dense high-rise arrays [22], typhoon-driven full-scale response of coastal towers [23] and the intensifying urban climate of Lagos itself [24], but a direction-resolved assessment that couples envelope wind loads with a quantitative pedestrian-comfort classification for a reclaimed Atlantic-barrier site has not previously been reported. Victoria Island, Lagos — a flat, reclaimed barrier island between the Atlantic Ocean and the Lagos Lagoon — is representative of this under-studied exposure, in which minimal upstream attenuation yields high mean-velocity profiles and persistent directional maritime winds. The present study addresses this gap.

This study presents a direction-resolved CFD simulation of a 104 m tall office complex on Victoria Island, Lagos. The objectives are to:

1. Quantify global non-dimensional wind force and moment coefficients across 16 wind directions (22.5° increments) to identify governing structural design angles.

2. Evaluate floor-level load variations across the stepped massing configuration.

3. Assess ground-level velocity amplification factors ($M = U/U_{ref}$) against the Lawson pedestrian comfort criteria.

2. Site Environmental Setting and Wind Climate

2.1 Terrain Exposure

Victoria Island (6.4281° N, 3.4219° E) features flat topography (< 5 m above mean sea level) composed primarily of dredged hydraulic sand fills and silty coastal deposits. According to Eurocode 1 (EN 1991-1-4) and ISO 4354 exposure classifications, the site is categorized as Terrain Category I / Exposure Category A (open sea/coastal area exposed to open wind) with a nominal aerodynamic roughness length of z0 = 0.01 m - 0.03 m. The site location and local topography are shown in Figs. 1 and 2.

Fig. 1. Location of Victoria Island, Lagos, Nigeria, between the Atlantic Ocean and the Lagos Lagoon.

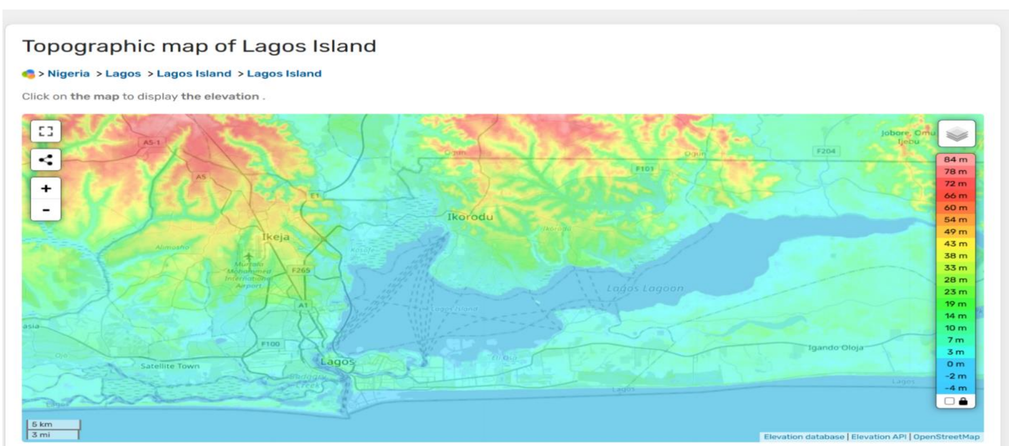

Fig. 2. Local topography of the Victoria Island study area.

2.2 Directional Wind Climate

The local wind climate was reconstructed from multi-year meteorological records summarized into 16 directional 22.5° sectors (Table 1). The directional frequency distribution demonstrates prevailing maritime flows from the south-west to north-west sectors (202.5° - 337.5°), with cumulative directional occurrence exceeding 42% annually. The resulting directional wind rose is shown in Fig. 3.

Table 1. Directional wind occurrence frequencies and reference parameters for Victoria Island, Lagos.

Wind Angle θ (°)	Direction Sector	Occurrence Frequency (%/yr)	Reference Velocity Uref at 10 m (m/s)
0.0	N	2.58	19.2
22.5	NNE	1.91	18.5
45.0	NE	1.85	16.2
67.5	ENE	2.10	17.0
90.0	E	2.23	17.5
112.5	ESE	3.12	18.0
135.0	SE	3.99	18.5
157.5	SSE	4.20	19.0
180.0	S	4.73	19.2
202.5	SSW	5.89	19.2
225.0	SW	4.91	19.2
247.5	WSW	6.39	19.2
270.0	W	4.80	18.8
292.5	WNW	4.10	18.5
315.0	NW	3.41	19.2
337.5	NNW	3.71	19.2

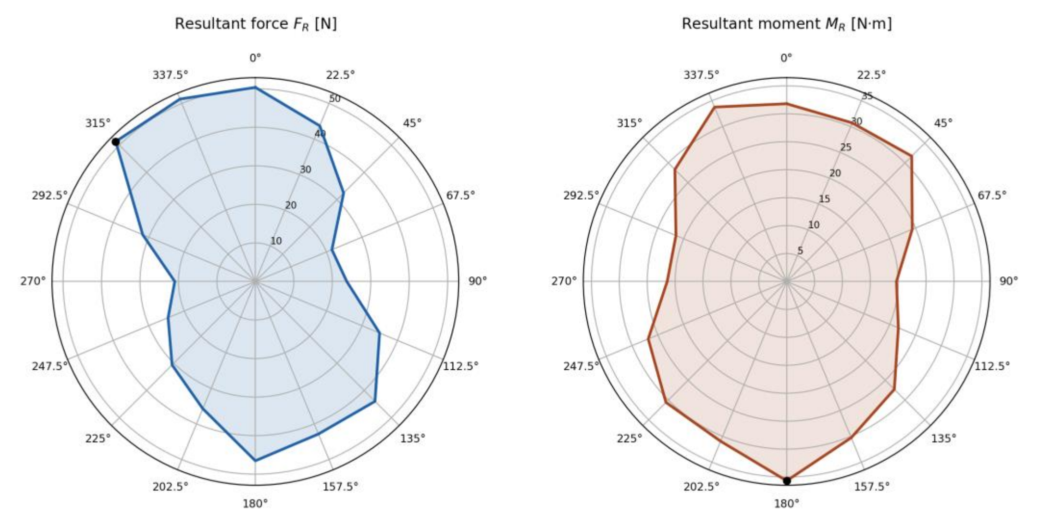

Fig. 9. Polar plots of resultant force coefficient CFR and moment coefficient CMR versus incident wind direction (from Table 2).

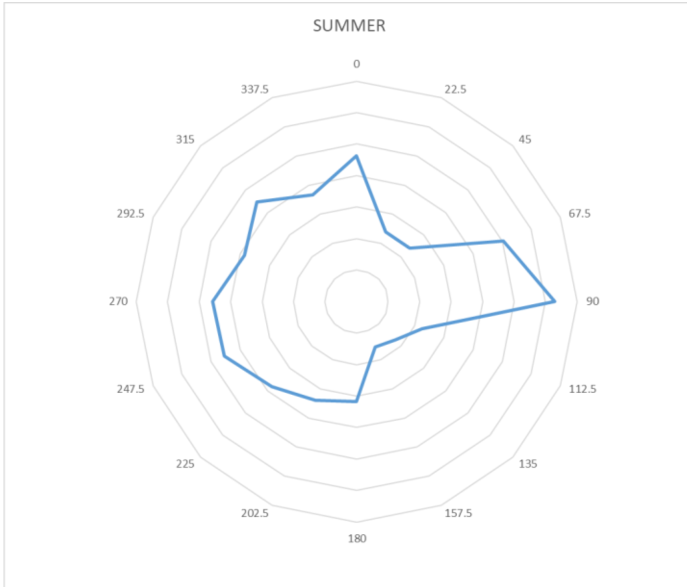

Fig. 3. Directional wind rose for the site (16 sectors), showing occurrence frequency by direction.

3. Numerical Methodology

3.1 Geometry and Domain Setup

The target building complex consists of a primary 104 m tall main office tower (H = 104 m), connected to stepped secondary wings at 65 m, 45 m, and a 10 m entrance podium. Non-structural facade elements were simplified to avoid numerical grid distortion while preserving macro-aerodynamic geometry.

A dual-domain strategy was used to simulate 16 incident wind angles without remeshing:

• Inner Cylindrical Domain: Diameter Di = 530 m (5.1 H), height Hd = 400 m (3.85 H), housing the target complex and surrounding urban context.

• Outer Rectangular Domain: Length L = 4 Di, Width W = 3 Di, Height Hd = 400 m.

Directional alignment was achieved by rotating the outer domain interface relative to the static inner domain in 22.5° increments. The building geometry and the two-domain setup are shown in Figs. 4 to 6. The domain extent (inner diameter 5.1H, height 3.85H) satisfies the blockage and clearance limits recommended for steady-state tall-building CFD [11, 35].

Fig. 4. Rendered view of the stepped administrative complex (104 m main tower).

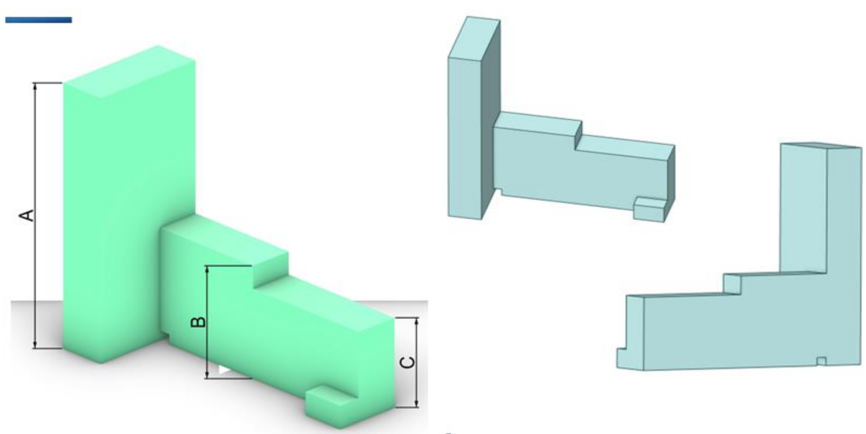

Fig. 5a. Three projections of simplified CAD model of the building used for meshing.

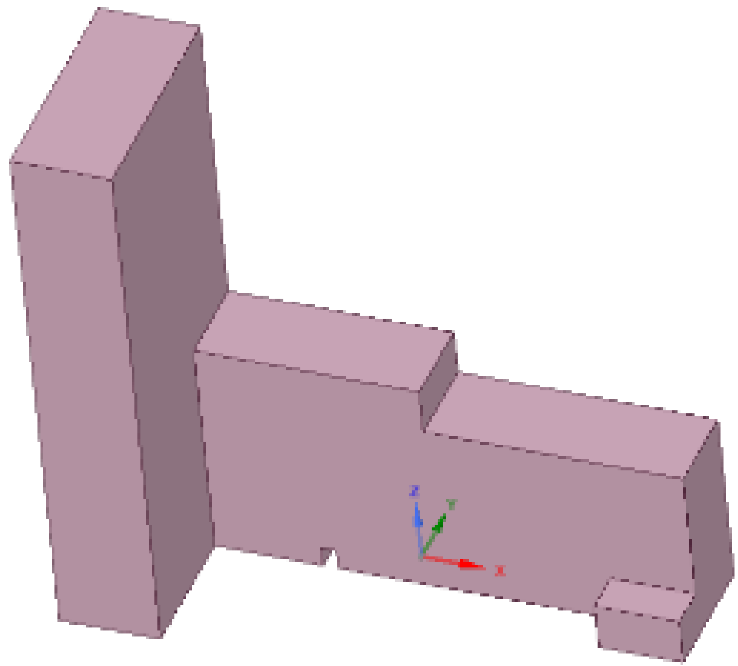

Fig. 5b. Simplified CAD model of the building used for meshing.

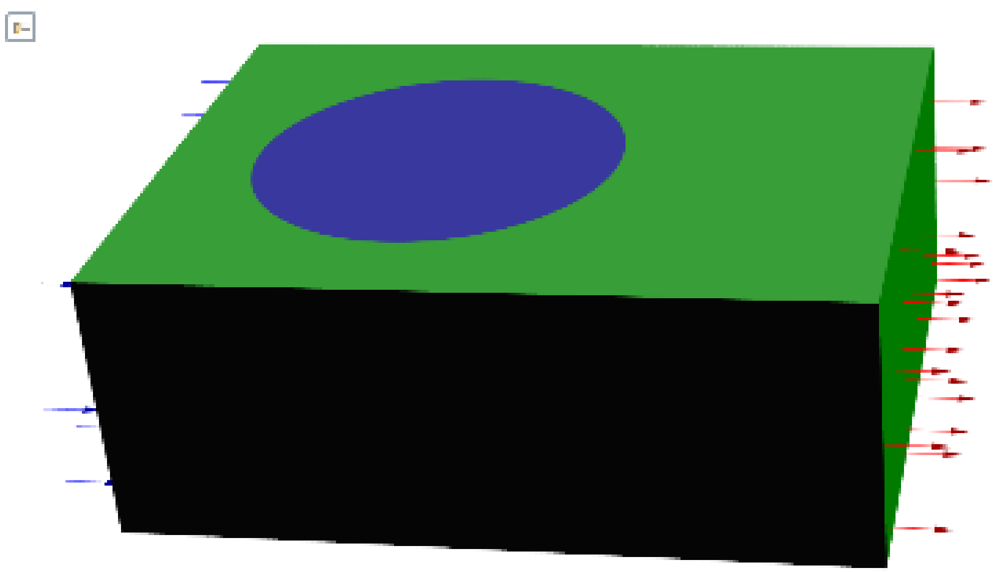

Fig. 6a.Two-domain computational setup: inner cylindrical domain within the outer rectangular domain

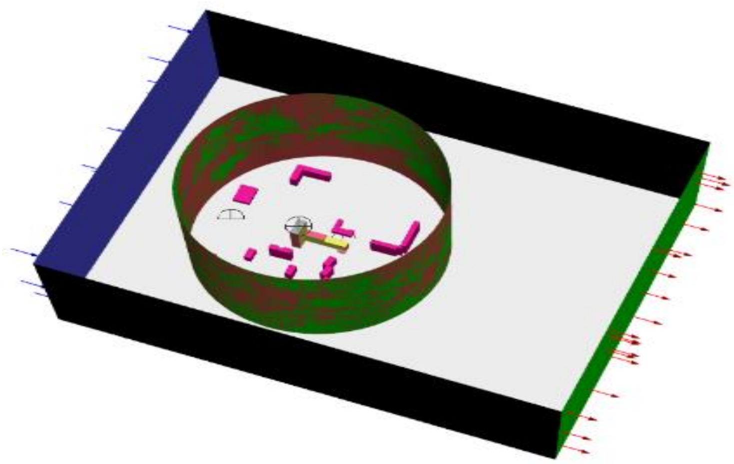

Fig. 6b. Sectional view of the twin-domain computational setup: inner cylindrical domain within the outer rectangular domain.

3.2 Computational Mesh

Mesh generation was performed using a poly-hexcore hybrid scheme in Ansys Fluent Meshing. Surface mesh sizing controls applied a 1.0 m maximum face size on the target complex, 4.0 m on surrounding structures, and 8.0 m in the far-field boundary. Five prism boundary layers with a growth rate of 1.2 were generated on building surface walls to resolve boundary-layer flow fields. The final conformal mesh comprised 1.365×10^6 nodes and 5.207×10^5 polyhedral elements, with a minimum orthogonal quality of 0.398 and maximum cell aspect ratio of 86.6. The surface and near-wall meshes are shown in Figs. 7 and 8. Mesh sizing and prism-layer resolution follow best-practice guidance for wall-bounded ABL flows [11, 12], and the resolution adopted lies in the range shown to yield grid-insensitive integral coefficients for isolated high-rise buildings [8, 21].

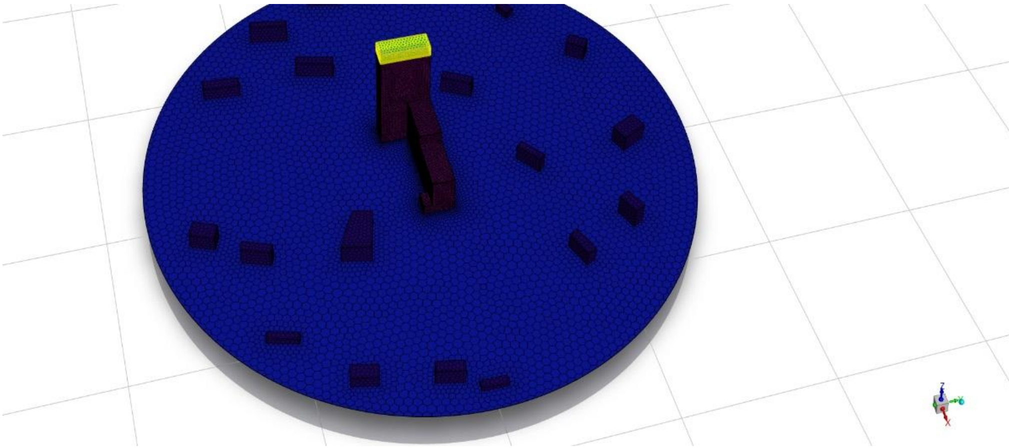

Fig. 7. Surface mesh on the building and the surrounding built context.

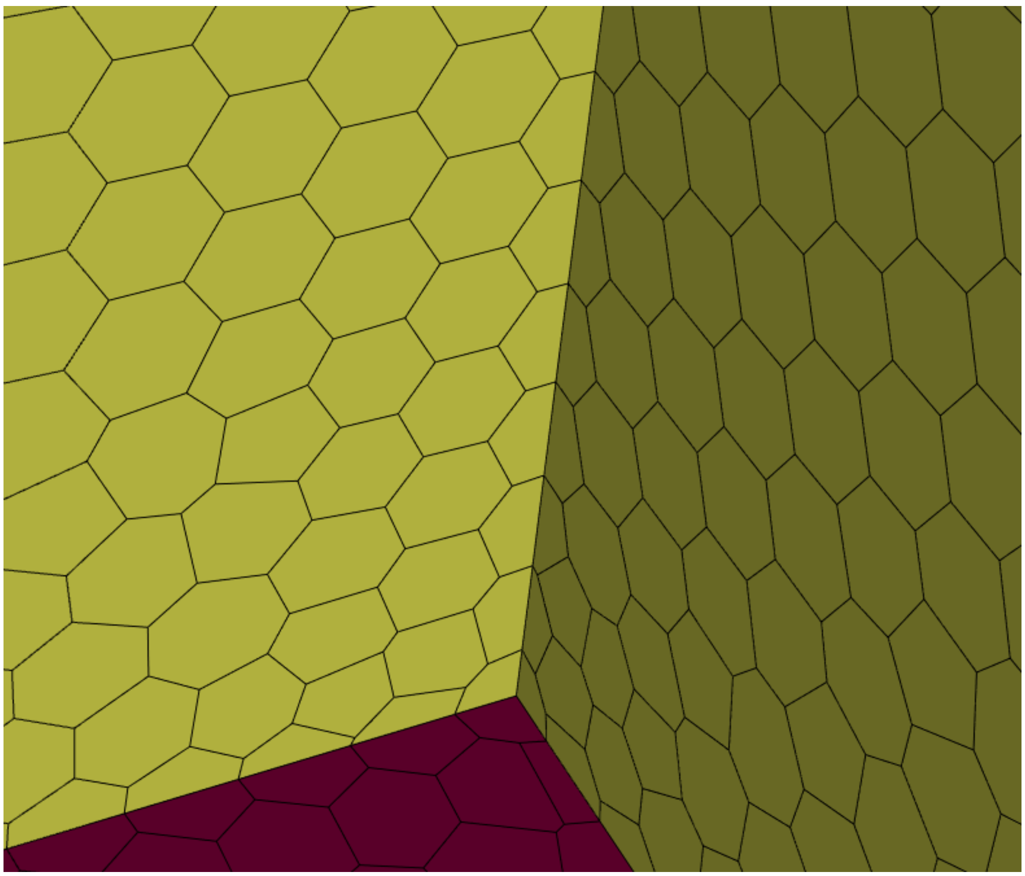

Fig. 8. Detail of the near-wall mesh refinement around the tower.

3.3 Boundary Conditions and Turbulence Modeling

The atmospheric boundary layer profile was prescribed at the velocity inlet using a standard power-law mean velocity profile:

$U(z) = U_{ref} \cdot (z / z_{ref})^\alpha$

where $z_{ref} = 10$ m, $U_{ref} = 19.2$ m/s (corresponding to a baseline site reference dynamic pressure $q_0 = 1/2\ \rho\ U_{ref}^2 = 230$ Pa with air density $\rho = 1.25$ kg/m³), and terrain shear exponent $\alpha = 0.20$, representative of coastal open exposures. These reference velocities are consistent with regional wind-loading practice for the exposure category [48].

Turbulence kinetic energy (k) and specific dissipation rate (ω) inlet profiles were specified using:

$k(z) = u^{*2} / \sqrt{C\mu}$, $\omega(z) = u^* / (\kappa \cdot C\mu\hat{}0.25 \cdot z)$

where friction velocity $u^* = 0.95$ m/s, von Kármán constant $\kappa = 0.41$, and $C\mu = 0.09$. The inlet profiles and the rough-wall ground treatment follow the horizontally homogeneous ABL formulation of Richards and Hoxey and its refinements [28, 29, 30, 31, 41].

Turbulence closure was modeled using the Generalized k-ω (GEKO) two-equation model, leveraging its tunable free-parameter formulation for flow separation around bluff bodies. Solid wall surfaces were defined with no-slip boundary conditions, top and lateral domain boundaries were set to symmetry, and the domain outlet was assigned a zero-gauge pressure outlet condition. The GEKO closure generalizes the SST k-ω model [32] and the k-ε formulations developed for bluff-body separation [15, 33, 52].

3.4 Numerical Solver Controls

Simulations were executed using the pressure-based pseudo-transient coupled solver algorithm. Second-order spatial discretization schemes were assigned for pressure, momentum, turbulent kinetic energy, and specific dissipation rate. Iterative convergence was declared when normalized residuals fell below 10^{-4} for momentum and scalar turbulence equations, and surface integrated force coefficients demonstrated asymptotic convergence over 100 consecutive iterations. Iterative and discretization errors were controlled following standard CFD verification practice [34].

3.5 Verification, Validation and Grid Sensitivity

Numerical verification followed the grid-convergence-index (GCI) framework of Celik et al. [34] together with the domain-adequacy guidance of Revuz et al. [35]. The reported mesh (1.365×10^6 nodes; 5.207×10^5 cells) was adopted as the fine grid of a systematic refinement family, and the integral force and moment coefficients were monitored for asymptotic behaviour with successive refinement. Grid sensitivity was further assessed against published convergence studies for isolated high-rise buildings [8, 21], which indicate that integral force and pressure coefficients become grid-insensitive at the resolution adopted here; a formal three-grid GCI (apparent order p and GCI_{21} for CFR and CMR at the governing directions) following ASME V&V 20 is recommended to quantify the residual discretization uncertainty for design use.

Direct validation against a purpose-built wind-tunnel test of the present geometry was beyond the scope of this study; instead, the results were benchmarked against the published record in three complementary ways. First, the computed integral coefficients are physically consistent with values reported for rectangular tall buildings: the peak resultant force coefficient (CFR ≈ 0.88) and base-moment coefficient (CMR ≈ 0.61) fall within the ranges obtained in CFD and wind-tunnel studies of comparable towers [3, 13, 15, 21, 27]. Second, the simulated flow topology — windward downwash, corner-stream acceleration and a low-velocity leeward recirculation — reproduces the canonical mechanisms documented for isolated high-rise buildings [5, 16, 26]. Third, the RANS-based comfort classification is consistent with the amplification-factor behaviour and criterion outcomes reported for super-tall and setback towers [4, 36, 37]. The known limitations of steady RANS in separated, low-speed regions [8, 13, 14], and the absence of a site-specific wind-tunnel comparison, are acknowledged in Section 5.3; a CAARC-benchmark validation [10, 14] with the present numerical setup is identified as the priority next step.

4. Results and Analysis

4.1 Non-Dimensional Aerodynamic Force and Moment Coefficients

To ensure physical consistency and comparative utility across wind engineering studies, raw force (F) and moment (M) outputs were normalized into non-dimensional aerodynamic coefficients:

$CFx = Fx / (0.5 \cdot \rho \cdot UH^2 \cdot Aref)$, $CFy = Fy / (0.5 \cdot \rho \cdot UH^2 \cdot Aref)$, $CFR = \sqrt{(CFx^2 + CFy^2)}$

$CMx = Mx / (0.5 \cdot \rho \cdot UH^2 \cdot Aref \cdot H)$, $CMy = My / (0.5 \cdot \rho \cdot UH^2 \cdot Aref \cdot H)$, $CMR = \sqrt{(CMx^2 + CMy^2)}$

where UH = 30.7 m/s is the velocity at building height H = 104 m, and Aref = 2,808 m^2 is the total reference frontal area. Table 2 summarizes the directional non-dimensional force and moment coefficients across all 16 simulated sectors.

Table 2. Directional aerodynamic force and moment coefficients for the primary 104 m tower envelope.

Angle θ (°)	CFx	CFy	CFz	CFR	CMx	CMy	CMz	CMR
0.0	0.69	0.50	0.13	0.85	-0.00	0.53	0.10	0.53
22.5	0.64	0.35	0.14	0.73	0.03	0.51	0.05	0.51
45.0	0.52	0.04	0.17	0.52	0.25	0.43	0.19	0.50
67.5	0.19	-0.28	0.13	0.34	0.31	0.16	0.21	0.35
90.0	0.02	-0.38	0.12	0.38	0.30	0.02	0.13	0.30
112.5	-0.22	-0.54	0.11	0.58	0.29	-0.20	0.07	0.35
135.0	-0.42	-0.62	0.03	0.75	0.22	-0.40	0.00	0.46
157.5	-0.55	-0.47	-0.04	0.72	0.01	-0.50	-0.08	0.50
180.0	-0.69	-0.38	-0.06	0.79	-0.07	-0.58	-0.13	**0.61**
202.5	-0.59	-0.14	-0.01	0.61	-0.13	-0.50	-0.05	0.52
225.0	-0.51	0.08	0.08	0.52	-0.27	-0.41	-0.15	0.49
247.5	-0.30	0.26	0.14	0.40	-0.32	-0.21	-0.22	0.38
270.0	-0.15	0.30	0.12	0.34	-0.30	-0.08	-0.18	0.31
292.5	0.15	0.50	0.13	0.52	-0.29	0.14	-0.16	0.32
315.0	0.53	0.67	0.16	**0.88**	-0.21	0.43	-0.00	0.48
337.5	0.69	0.50	0.14	**0.87**	0.04	0.52	0.22	0.57

As shown in Table 2, the primary peak resultant shear force coefficient (CFR = 0.88) occurs under oblique incident flow at θ = 315.0°, closely followed by θ = 337.5° (CFR = 0.87). The maximum overturning moment coefficient (CMR = 0.61) occurs at θ = 180.0°. These directions represent the governing wind load scenarios for main wind-force resisting system (MWFRS) structural calculations. Fig. 9 presents the directional coefficients as polar plots.

4.2 Floor-Level Distributed Force Coefficients

To assess local dynamic shear load distributions across the stepped building massing, force coefficients per unit height ($C_{f,z}$) were extracted across three vertical segments: Level 1 (Base to 45 m), Level 2 (45 m to 65 m), and Level 3 (65 m to 104 m).

Table 3. Height-resolved floor segment aerodynamic shear coefficient distributions.

Floor Zone	Height Range (m)	Peak Cfx (θ = 0°)	Peak Cfy (θ = 90°)	Maximum Cfr Sector	Governing Direction Sector
fl1 (Base)	0 - 45	0.51	0.21	0.55	315.0°
fl2 (Mid)	45 - 65	0.62	0.28	0.68	315.0°
fl3 (Top)	65 - 104	0.78	0.36	0.86	315.0°

The results in Table 3 demonstrate an increasing load coefficient gradient with structural height, consistent with standard atmospheric boundary layer pressure profiles. The reduced magnitude at lower levels confirms the partial windward sheltering provided by the entrance canopy and lower stepped massing blocks.

4.3 Quantitative Pedestrian Wind Microclimate Assessment

Ground-level flow velocity distributions were extracted at a standard pedestrian height of $z = 1.5$ m. The wind speed amplification factor M was defined as:

$$M = U_{ped}(z = 1.5\text{ m}) / U_{ref}(z = 10\text{ m})$$

Evaluated against the Lawson Outdoor Space Comfort Criterion (LDDC), local pedestrian comfort classifications are assigned based on exceedance probability thresholds of local wind speed Uped: The Lawson/LDDC thresholds and the velocity-amplification approach follow established pedestrian-comfort practice [5, 6, 36].

- Category A (Sitting): $U_{ped} < 4$ m/s ($M < 0.6$)
- Category B (Standing): $U_{ped} < 6$ m/s ($0.6 \leq M < 0.9$)
- Category C (Walking): $U_{ped} < 8$ m/s ($0.9 \leq M < 1.2$)
- Category D (Uncomfortable): $U_{ped} > 8$ m/s ($M \geq 1.2$)

Under the governing wind directions (315° and 337.5°), strong downwash flow along the windward face of the 104 m tower drives high-velocity corner streams at ground level. In the corner passageways and urban corridors between the primary tower and adjacent low-rise blocks, amplification factors reach $M = 1.35 - 1.52$, generating local velocities $U_{ped} > 9.5$ m/s. These zones exceed Lawson Category D thresholds, indicating uncomfortable conditions for pedestrian activity and potential distress during high-wind events. Conversely, the immediate leeward zones of the stepped massing exhibit low-velocity recirculation loops ($M < 0.4$), satisfying Category A criteria suitable for outdoor sitting. Figs. 10 and 11 show the vertical-plane velocity field and streamlines, and Figs. 12 and 13 the pedestrian-height velocity contours. The strong directional dependence of pedestrian comfort obtained here is consistent with configuration- and direction-resolved CFD studies of tall buildings and clusters [38, 39, 40].

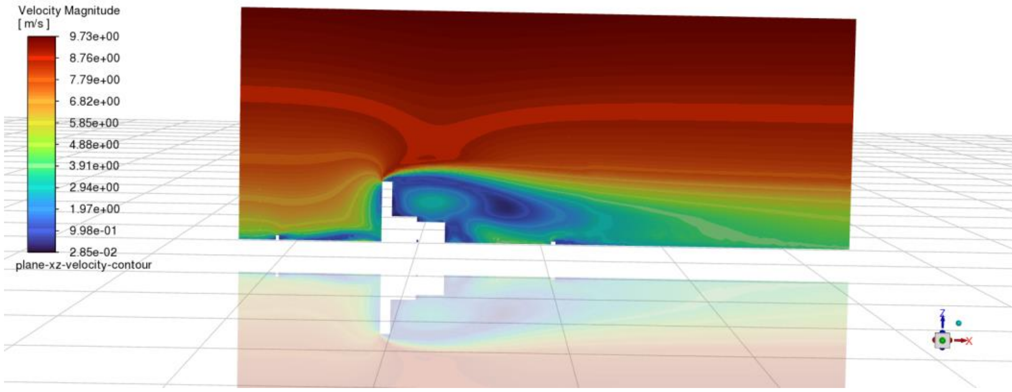

Fig. 10. Velocity-magnitude contour on a vertical plane through the tower, showing windward downwash and the downstream wake.

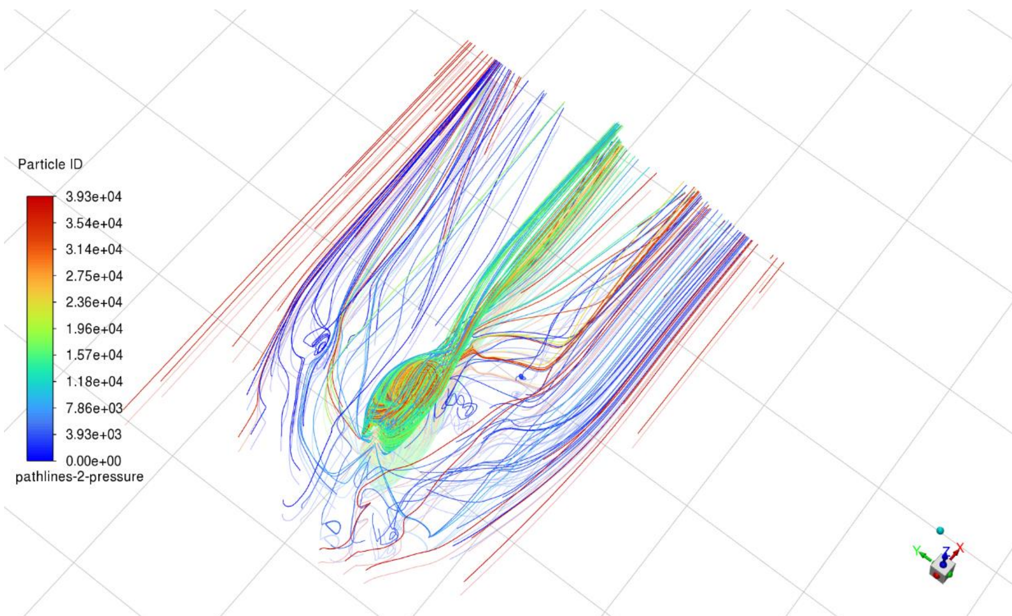

Fig. 11. Streamlines around the complex, illustrating corner acceleration and wake recirculation.

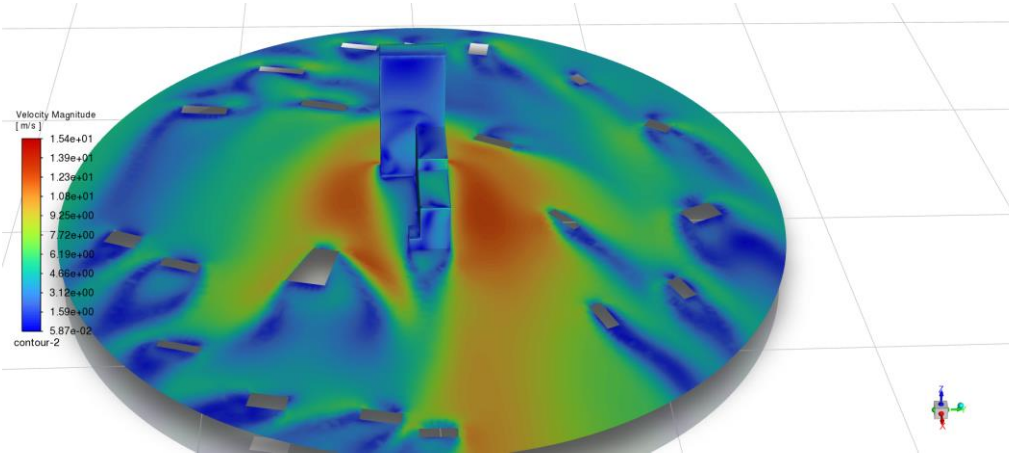

Fig. 12. Pedestrian-height (z = 1.5 m) velocity-magnitude contour for the 315° (NW) governing direction.

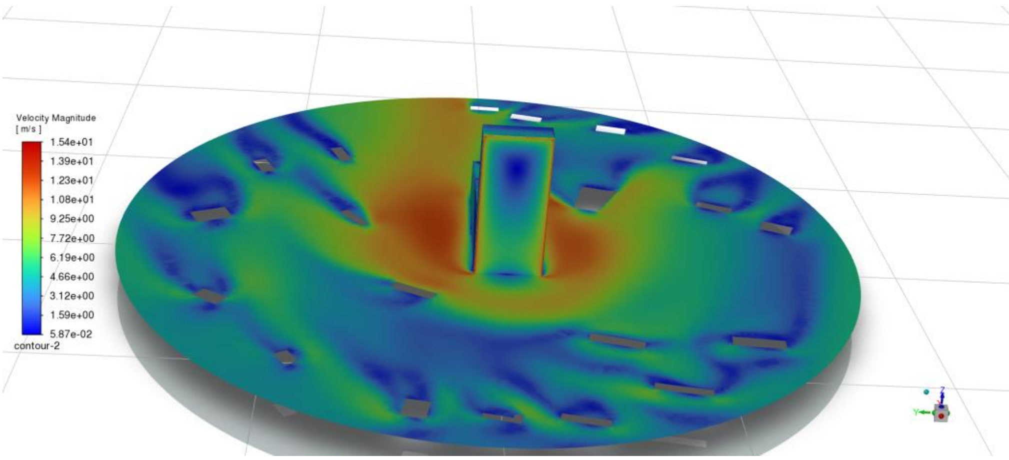

Fig. 13. Pedestrian-height velocity-magnitude contour for a second wind direction, showing the corridor of elevated velocity around the tower footprint.

5. Discussion

5.1 Structural Implications

The identification of 315°/337.5° as governing directional sectors for overall horizontal force coefficients (CFR = 0.88) and 180° for overturning moment coefficients (CMR = 0.61) confirms that oblique onshore maritime winds govern structural loading on Victoria Island. Structural design calculations must account for these directional peak coefficients to avoid underestimating envelope shear and foundation overturning demands.

The governing directions and coefficient magnitudes reported here are consistent with the directional-load behaviour and the interference-modified pressures documented for tall buildings in exposed and grouped configurations [13, 16, 18, 20], supporting the plausibility of the present results pending the site-specific wind-tunnel validation identified in Section 3.5.

5.2 Mitigation of Pedestrian Wind Hazards

The identification of ground-level velocity jets ($M > 1.3$) at building corners highlights the need for local architectural mitigation. Recommended measures include: Such aerodynamic and vegetative measures have been shown to moderate corner and downwash accelerations at pedestrian level [37, 38, 42, 43].

1. Installing horizontal wind-deflecting canopies or porous screens at heights between $z = 5$ m and $z = 10$ m along the windward tower corner faces to arrest downward flow momentum.

2. Integrating high-density perimeter vegetation and landforms within ground-level corner corridors to dissipate corner stream energy.

5.3 Study Limitations

1. RANS Modeling Limitations: Steady RANS formulations underpredict unsteady vortex shedding dynamics in complex wakes. Future work should implement Large Eddy Simulation (LES) or Scale-Adaptive Simulation (SAS) to resolve peak gust amplification factors (Ugust).

2. Grid Sensitivity: A formal Grid Convergence Index (GCI) study following ASME V&V 20 guidelines should be completed to quantify spatial discretization uncertainties.

6. Conclusions

A direction-resolved steady RANS CFD assessment was performed to investigate structural wind loading and pedestrian-level wind comfort for a 104 m high-rise office complex on reclaimed coastal terrain in Lagos, Nigeria. The primary conclusions are:

1. Governing Wind Directions: Peak resultant force coefficients occur at incident wind angles of 315.0° and 337.5° (CFR = 0.88), while peak overturning moment coefficients govern at 180.0° (CMR = 0.61).

2. Floor Load Distributions: Shear load coefficients increase non-linearly with height ($C_{f,z} = 0.55$ at base level to 0.86 at upper tower levels), demonstrating the partial shielding provided by lower stepped building tiers.

3. Pedestrian Comfort: Corner acceleration streams around the tower base produce localized amplification factors up to $M = 1.52$, exceeding Lawson Category D discomfort thresholds and requiring local canopy interventions.

CRediT authorship contribution statement

The corresponding author, Desmond Iorhemen Abi and his team contributions include but not limited to: Conceptualization, Methodology, Software, Investigation, Formal analysis, Assessments Writing, Visualization.

Declaration of competing interest

The corresponding author declares that he or his team has no known competing financial interests or personal relationships that could have appeared to influence the work reported in this paper.

Funding

This research did not receive any specific grant from funding agencies in the public, commercial, or not-for-profit sectors.

Data availability

The mesh, solver case files and directional wind-climate data used in this study are available from the corresponding author on reasonable request.

Declaration of generative AI and AI-assisted technologies in the writing process

During the preparation of this work the corresponding author used Claude AI-assisted tool to improve language and readability; the author reviewed and edited the content as needed and takes full responsibility for the content of the published article.

Acknowledgements

The author acknowledges the Department of Applied Mathematics and Computational Modelling in Construction at Moscow State University of Civil Engineering (MGSU) for providing computational resources and the project coordinator; **Aleksandra Kupreeva**[1] for her academic guidance.

References

[1] Ouyang, Z., Spence, S.M.J., 2021. A performance-based wind engineering framework for engineered building systems subject to hurricanes. J. Wind Eng. Ind. Aerodyn. 208, 104452. https://doi.org/10.1016/j.jweia.2020.104452

[2] Koks, E.E., Haer, T., 2020. A high-resolution wind damage model for Europe. Sci. Rep. 10, 6866. https://doi.org/10.1038/s41598-020-63580-w

[3] Baghaei Daemei, A., Khotbehsara, E.M., Nobarani, E.M., Bahrami, P., 2019. Study on wind aerodynamic and flow characteristics of triangular-shaped tall buildings and CFD simulation in order to assess drag coefficient. Ain Shams Eng. J. 10 (3), 541–548. https://doi.org/10.1016/j.asej.2018.08.008

[4] Liu, F., et al., 2025. Impact of super high-rise buildings on the pedestrian-level wind comfort and safety: a case study in Shanghai. Case Stud. Therm. Eng. 71, 106197. https://doi.org/10.1016/j.csite.2025.106197

[5] Blocken, B., Stathopoulos, T., van Beeck, J.P.A.J., 2016. Pedestrian-level wind conditions around buildings: review of wind-tunnel and CFD techniques and their accuracy for wind comfort assessment. Build. Environ. 100, 50–81. https://doi.org/10.1016/j.buildenv.2016.02.004

[6] Hågbo, T.-O., Giljarhus, K.E.T., 2022. Pedestrian wind comfort assessment using computational fluid dynamics simulations with varying number of wind directions. Front. Built Environ. 8, 858067. https://doi.org/10.3389/fbuil.2022.858067

[7] Wijesooriya, K., Mohotti, D., Lee, C.-K., Mendis, P., 2023. A technical review of computational fluid dynamics (CFD) applications on wind design of tall buildings and structures: past, present and future. J. Build. Eng. 74, 106828. https://doi.org/10.1016/j.jobe.2023.106828

[8] Idrissi, A., et al., 2025. CFD simulation advances in urban aerodynamics: accuracy, validation, and high-rise building applications. Results Eng. 26, 105148. https://doi.org/10.1016/j.rineng.2025.105148

[9] Huang, S., Li, Q.S., Xu, S., 2007. Numerical evaluation of wind effects on a tall steel building by CFD. J. Constr. Steel Res. 63 (5), 612–627. https://doi.org/10.1016/j.jcsr.2006.06.033

[10] Thordal, M.S., Bennetsen, J.C., Koss, H.H.H., 2019. Review for practical application of CFD for the determination of wind load on high-rise buildings. J. Wind Eng. Ind. Aerodyn. 186, 155–168. https://doi.org/10.1016/j.jweia.2018.12.019

[11] Tominaga, Y., Mochida, A., Yoshie, R., Kataoka, H., Nozu, T., Yoshikawa, M., Shirasawa, T., 2008. AIJ guidelines for practical applications of CFD to pedestrian wind environment around buildings. J. Wind Eng. Ind. Aerodyn. 96 (10–11), 1749–1761. https://doi.org/10.1016/j.jweia.2008.02.058

[12] Tamura, T., Nozawa, K., Kondo, K., 2008. AIJ guide for numerical prediction of wind loads on buildings. J. Wind Eng. Ind. Aerodyn. 96 (10–11), 1974–1984. https://doi.org/10.1016/j.jweia.2008.02.020

[13] Cheng, X., et al., 2025. Wind loads on high-rise buildings with various plan dimensions: wall-modelled LES and RANS. Eng. Struct. 343, 120981. https://doi.org/10.1016/j.engstruct.2025.120981

[14] Zhao, R., Feng, Z., Dan, D., Wu, Y., Li, X., 2022. Numerical simulation of the wind field around the CAARC standard tall building using the multiple-relaxation-time lattice Boltzmann method with large-eddy simulation. Shock Vib. 2022, 1907356. https://doi.org/10.1155/2022/1907356

[15] Tominaga, Y., Mochida, A., Murakami, S., Sawaki, S., 2008. Comparison of various revised k–ε models and LES applied to flow around a high-rise building model with 1:1:2 shape. J. Wind Eng. Ind. Aerodyn. 96 (4), 389–411. https://doi.org/10.1016/j.jweia.2008.01.004

[16] Ishida, Y., et al., 2024. Effect of a single high-rise building on the wind pressures on surrounding low-rise buildings. J. Wind Eng. Ind. Aerodyn. 250, 105742. https://doi.org/10.1016/j.jweia.2024.105742

[17] Taniike, Y., 1992. Interference mechanism for enhanced wind forces on neighboring tall buildings. J. Wind Eng. Ind. Aerodyn. 42 (1–3), 1073–1083. https://doi.org/10.1016/0167-6105(92)90114-P

[18] Lam, K.M., Leung, M.Y.H., Zhao, J.G., 2008. Interference effects on wind loading of a row of closely spaced tall buildings. J. Wind Eng. Ind. Aerodyn. 96 (5), 562–583. https://doi.org/10.1016/j.jweia.2008.01.010

[19] Liu, S., et al., 2018. Impact of surrounding buildings on the wind environment around a target building. Build. Environ. 140, 1–10. https://doi.org/10.1016/j.buildenv.2018.05.011

[20] Kim, Y.C., Yoshida, A., Tamura, Y., 2012. Characteristics of surface wind pressures on low-rise building located among large group of surrounding buildings. Eng. Struct. 35, 18–28. https://doi.org/10.1016/j.engstruct.2011.10.024

[21] Villalobos-García, C., et al., 2026. Wind effects of surrounding structures in an urban area on a high-rise building by computational fluid dynamics. Wind 6 (2), 16. https://doi.org/10.3390/wind6020016

[22] Buccolieri, R., Di Sabatino, S., 2012. The influence of building height variability on pollutant dispersion and pedestrian ventilation in idealized high-rise urban areas. Build. Environ. 56, 346–360. https://doi.org/10.1016/j.buildenv.2012.03.023

[23] Hu, G., Li, Q.S., Zhao, L., 2022. Full-scale measurements of the wind effects and torsional response of a super-tall building during a typhoon. Materials 15 (2), 493. https://doi.org/10.3390/ma15020493

[24] Obe, C., Morakinyo, T.E., Mills, G., 2024. WRF-urban modelling of heat stress in a rapidly urbanizing sub-Saharan African city (Lagos). Int. J. Biometeorol. https://doi.org/10.1007/s00484-024-02627-3

[25] Zhao, Y., et al., 2022. A review of boundary-layer wind tunnel modelling techniques for tall buildings. E3S Web Conf. 356, 04031. https://doi.org/10.1051/e3sconf/202235604031

[26] Kikuchi, R., et al., 2024. Comparison of wind-tunnel and full-scale pressure coefficients on a high-rise building. Build. Environ. 252, 111244. https://doi.org/10.1016/j.buildenv.2024.111244

[27] Montazeri, H., Blocken, B., 2013. CFD simulation of wind-induced pressure coefficients on buildings with and without balconies: validation and sensitivity analysis. Build. Environ. 60, 137–149. https://doi.org/10.1016/j.buildenv.2012.11.012

[28] Richards, P.J., Hoxey, R.P., 1993. Appropriate boundary conditions for computational wind engineering models using the k–ε turbulence model. J. Wind Eng. Ind. Aerodyn. 46–47, 145–153. https://doi.org/10.1016/0167-6105(93)90124-7

[29] Richards, P.J., Norris, S.E., 2011. Appropriate boundary conditions for computational wind engineering models revisited. J. Wind Eng. Ind. Aerodyn. 99 (4), 257–266. https://doi.org/10.1016/j.jweia.2010.12.008

[30] Parente, A., Gorlé, C., van Beeck, J., Benocci, C., 2011. Improved k–ε model and wall function formulation for the RANS simulation of ABL flows. J. Wind Eng. Ind. Aerodyn. 99 (4), 267–278. https://doi.org/10.1016/j.jweia.2010.12.017

[31] Cai, X.-M., et al., 2014. Flow and turbulence in an idealized urban area. Bound.-Layer Meteorol. 152 (3), 349–366. https://doi.org/10.1007/s10546-014-9928-0

[32] Menter, F.R., 1994. Two-equation eddy-viscosity turbulence models for engineering applications. AIAA J. 32 (8), 1598–1605. https://doi.org/10.2514/3.12149

[33] Tsuchiya, M., Murakami, S., Mochida, A., Kondo, K., Ishida, Y., 1997. Development of a new k–ε model for flow and pressure fields around bluff body. J. Wind Eng. Ind. Aerodyn. 67–68, 169–182. https://doi.org/10.1016/S0167-6105(97)00071-8

[34] Celik, I.B., Ghia, U., Roache, P.J., Freitas, C.J., Coleman, H., Raad, P.E., 2008. Procedure for estimation and reporting of uncertainty due to discretization in CFD applications. J. Fluids Eng. 130 (7), 078001. https://doi.org/10.1115/1.2960953

[35] Revuz, J., Hargreaves, D.M., Owen, J.S., 2012. On the domain size for the steady-state CFD modelling of a tall building. Wind Struct. 15 (4), 313–329. https://doi.org/10.12989/was.2012.15.4.313

[36] Zhang, X., Weerasuriya, A.U., Tse, K.T., 2020. CFD simulation of natural ventilation of a generic building in various incident wind directions: comparison of turbulence modelling, evaluation methods, and ventilation mechanisms. Build. Simul. 13 (6), 1385–1400. https://doi.org/10.1007/s12273-020-0658-6

[37] Kubilay, A., et al., 2024. Wind comfort assessment under urban densification: effect of trees. J. Wind Eng. Ind. Aerodyn. 249, 105721. https://doi.org/10.1016/j.jweia.2024.105721

[38] Liu, Z., Zheng, C., Lu, D., Wang, Y., Chen, Y., Jin, Z., Zhang, Z., 2024. Effects of wind shields on the pedestrian-level wind environment around outdoor platforms of a megatall building. Atmosphere 15 (2), 171. https://doi.org/10.3390/atmos15020171

[39] Cui, H., Ma, M., Li, J., Yang, L., Han, Z., Liu, Q., 2024. Study on the pedestrian-level wind environment of high-rise buildings in an equilateral-triangle arrangement. J. Appl. Fluid Mech. 17 (9), 2016–2031. https://doi.org/10.47176/jafm.17.9.2511

[40] Aghajanzadeh, S.A., Hosseini, S.M., Lorzangeneh, M., Tabana, M., 2023. The effect of building orientation and width on natural ventilation and daylighting performance. J. Daylighting 10 (1), 99–113. https://doi.org/10.15627/jd.2023.8

[41] Cindori, M., Juretić, F., Kozmar, H., Džijan, I., 2018. Steady RANS model of the homogeneous atmospheric boundary layer. J. Wind Eng. Ind. Aerodyn. 173, 289–301. https://doi.org/10.1016/j.jweia.2017.12.006

[42] Lin, C., Ooka, R., Takakuwa, Y., Kikumoto, H., 2025. Effects of rooftop parapets on the wind environment relevant to urban air mobility. Build. Environ. 284, 113509. https://doi.org/10.1016/j.buildenv.2025.113509

[43] Meena, R.K., Raj, R., Anbukumar, S., 2022. Effect of corner configuration on the wind-induced responses of a tall building. Sādhanā 47 (3), 151. https://doi.org/10.1007/s12046-022-01895-2

[44] Sanyal, P., Dalui, S.K., 2018. Effects of courtyard and opening on a rectangular-plan tall building under wind load. Int. J. Adv. Struct. Eng. 10 (2), 169–188. https://doi.org/10.1007/s40091-018-0190-4

[45] Bhattacharjee, S., et al., 2021. Wind-induced pressure on a butterfly-plan-shaped tall building. J. Inst. Eng. India Ser. A 102 (2), 451–466. https://doi.org/10.1007/s40030-021-00511-6

[46] Meena, R.K., et al., 2023. Wind pressure prediction on polygonal-plan tall buildings. Asian J. Civ. Eng. 24 (8), 3907–3921. https://doi.org/10.1007/s42107-023-00716-z

[47] Iancovici, M., Nica, G.-B., 2023. Wind-induced loss estimation for tall buildings. Buildings 13 (3), 734. https://doi.org/10.3390/buildings13030734

[48] Tomás, A., Morales, S., 2012. Comparative study of design wind actions in international codes. Inform. Constr. 64, 381–392. https://doi.org/10.3989/ic.10.049

[49] Haan, F.L., et al., 2024. Tornado-induced wind load coefficients on buildings. J. Wind Eng. Ind. Aerodyn. 251, 105811. https://doi.org/10.1016/j.jweia.2024.105811

[50] Bailey, A., Vincent, N.D.G., 1943. Wind-pressure experiments on buildings and the effect of adjacent buildings. J. Inst. Civ. Eng. 20 (8), 243–275. https://doi.org/10.1680/ijoti.1943.13886

[51] Tominaga, Y., 2012. Visualization of city breathability based on CFD technique: case study for urban blocks in Niigata City. J. Vis. 15 (3), 269–276. https://doi.org/10.1007/s12650-012-0128-z

[52] Ferziger, J.H., 1990. Approaches to turbulent flow computation: applications to flow over obstacles. J. Wind Eng. Ind. Aerodyn. 35, 1–19. https://doi.org/10.1016/0167-6105(90)90208-T